A Hybrid Approach to 3D Microwave Imaging by Using Linear Sampling and Ant Colony Optimization

M. Brignone, G. Bozza, A. Randazzo, *Member, IEEE*, M. Piana, and M. Pastorino, *Senior Member, IEEE*

***Abstract*—In this paper a hybrid approach to inspect three-dimensional homogeneous dielectric scatterers by using microwaves is proposed. Namely, the considered method consists in two steps: first, the supports of the scatterers are retrieved by the Linear Sampling Method; then the permittivities of the targets are estimated by an Ant Colony Optimization algorithm. The described strategy combines the efficiency of the Linear Sampling Method with the global optimization capabilities of the stochastic procedure. Numerical results assess the capabilities of the approach also in the presence of noise.**

***Index Terms*—Inverse scattering, Linear Sampling Method, Ant Colony Optimization, stochastic methods**

I. Introduction

In the last years several methods have been proposed to solve the inverse scattering problems arising in microwave diagnostics, which finds application in several fields, ranging from non–destructive testing and evaluation (NDT/NDE) to medical imaging, and from civil engineering to target identification [1]–[6].

Current numerical methods for the solution of inverse scattering problems can be grouped into two families: *qualitative* and *quantitative* approaches.

Basically, qualitative methods construct a criterion to decide whether or not a point is in the support of the scatterers, so that they are able to detect shapes and positions of the targets under test. Usually, these methods are computationally highly efficent, but do not provide any information on the values of the electromagnetic parameters (dielectric permittivity, conductivity, and magnetic permeability.)

To this category belong the Linear Sampling Method (LSM) [7]–[9], the Reciprocity Gap Function (RGF) [10], the Synthetic Aperture Focusing Technique (SAFT) [11] and the Multiple Signal Classification (MUSIC) [12].

On the other hand, quantitative methods aim at determining the point values of the electromagnetic parameters and can be essentially divided into two categories: deterministic and stochastic approaches. The former are usually iterative methods [13]–[16], [20], computationally rather efficient, but they require specific actions to avoid local minima corresponding to false solutions (e.g., the iterative process must start with a trial solution not too far from the true solution.)

Stochastic methods usually recast the problem solution to the optimization of a suitable functional and are in principle able to reach the global minimum of this functional (see [21] and the references therein.) Common advantageous features of these techniques are the rich informative content of the restored map, but, unfortunately, their computational cost is usually very high.

In the last years, there has been a strong interest in developing hybrid strategies aimed at combining the positive features of two or more methods [17]–[19]. Following this trend, this paper presents for the first time the combination of a qualitative method, the Linear Sampling Method (LSM), with a stochastic optimization procedure, the Ant Colony Optimization (ACO) algorithm, for the imaging of three-dimensional scatterers.

More precisely, the imaging process is composed of two stages. In the first one, the shapes and positions of the dielectric scatterers are retrieved starting from the measured scattered field by using LSM. When the shapes of the targets inside the domain of interest are identified, the ACO method is applied to determine the dielectric properties of these targets, which are assumed here to be dielectrically homogeneous.

The LSM is proposed because of its robustness and generality: in fact it can be applied to an extremely wide class of scatterers (e.g., dielectric and perfectly electric conductor objects, weak and strong scatterers) without any *a priori* information [9], [22]. On the other hand, the Ant Colony Optimization has been used since in some applications it has been found to converge within a reasonably small number of iterations [21], [23].

The paper is organized as follows: in Section II the mathematical details of the two–step approach are discussed and the LSM and the ACO algorithm are described. In Section III several numerical results are presented to evaluate the capabilities and limitations of the method. Finally, Section IV draws some conclusions.

II. Mathematical Formulation

Let $T \subset \mathbb{R}^3$ be a space region containing N_{scatt} scatterers to be inspected, each of which is supposed to be non–magnetic and homogeneous. Accordingly, ε_{r_j} and σ_j denote the relative (real) dielectric permittivity and the electric conductivity of the j-th scatterer, respectively ($e^{-\mathrm{i}\omega t}$ time dependence is assumed and hereafter omitted.)

Manuscript received March 14, 2008.

M. Brignone and M. Piana are with the Dipartimento di Informatica, Università di Verona, Verona, Italia. e-mail: brignone@dima.unige.it, piana@sci.univr.it

G. Bozza, A. Randazzo, and M. Pastorino are with the Dipartimento di Ingegneria Biofisica ed Elettronica, Università di Genova, Genova, Italia. e-mail: {bozza, randazzo, pastorino}@dibe.unige.it

If the targets are illuminated by the incident electric field $\vec{E}_{inc}$, the total electric field $\vec{E}$ can then be determinated by solving the integral equation [25]

$$\begin{aligned}&\vec{E}(\vec{r}) - \vec{E}_{inc}(\vec{r}) = \\ &= -k_0^2 \sum_{j=1}^{N_{scatt}} \left(\varepsilon_{r_j} + \mathrm{i}\frac{\sigma_j}{\omega\varepsilon_0} - 1\right) \int_{D_j} \vec{\vec{G}}(\vec{r} \mid \vec{r}') \cdot \vec{E}(\vec{r}')d\vec{r}',\end{aligned} \tag{1}$$

where, being ε_0 the dielectric permittivity and μ_0 the magnetic permeability of the vacuum, $k_0 = \omega\sqrt{\varepsilon_0\mu_0}$ is the vacuum wavenumber, $\vec{\vec{G}}$ is the dyadic Green tensor, and $D_j \subset T$ denotes the support of the j-th scatterer. Hereafter, we will indicate by $\mathbf{D} = [D_1, \ldots, D_{N_{scatt}}]$, $\boldsymbol{\varepsilon}_r = [\varepsilon_{r_1}, \ldots, \varepsilon_{r_{N_{scatt}}}]$ and $\boldsymbol{\sigma} = [\sigma_1, \ldots, \sigma_{N_{scatt}}]$ the supports, the relative permittivities and the electric conductivities of the inspected scatterers, respectively. Moreover, we refer to $D = \cup_{j=1}^{N_{scatt}} D_j$ as the region occupied by all the scatterers.

As it is well known [26], [27], the scattered field $\vec{E}_{scatt} = \vec{E} - \vec{E}_{inc}$ has the asymptotic behavior

$$\vec{E}_{scatt}(\vec{r}) = \frac{e^{\mathrm{i}k_0 r}}{r}\left\{\vec{E}_\infty(\hat{r}) + \mathcal{O}\left(\frac{1}{r}\right)\right\}, \tag{2}$$

where $r = |\vec{r}|$ and $\hat{r} = \vec{r}/r$. It is worth remarking that the *far-field pattern* $\vec{E}_\infty$ is a tangential vector field, i.e. it belongs to the Hilbert space $L_t^2(\Omega) = \{\vec{f} \in (L^2(\Omega))^3 : \vec{f} \cdot \vec{n} = 0\}$, where $\vec{n}$ is the normal unit vector to the unit sphere $\Omega = \{\vec{r} \in \mathbb{R}^3,\ |\vec{r}| = 1\}$, equipped with the scalar product defined for every $\vec{f}_1, \vec{f}_2 \in L_t^2(\Omega)$ by

$$\left(\vec{f}_1(\cdot)\,,\, \vec{f}_2(\cdot)\right)_{L_t^2(\Omega)} = \int_\Omega \vec{f}_1(\hat{r}) \cdot \vec{f}_2(\hat{r})\, ds(\hat{r}). \tag{3}$$

Let us consider the unknown targets illuminated by an incident plane wave impinging from direction

$$\hat{d} = \sin\theta_d \cos\phi_d \hat{x} + \sin\theta_d \sin\phi_d \hat{y} + \cos\theta_d \hat{z}, \tag{4}$$

being $\hat{x}$, $\hat{y}$, $\hat{z}$ the cartesian unit vectors, $\theta_d \in [0, \pi]$, $\phi_d \in [0, 2\pi)$, and polarized along the vector $\vec{p}$, such that $\vec{p} \cdot \hat{d} = 0$. The incident wave can then be written as $\vec{E}_{inc}(\vec{r}) = \vec{p}e^{\mathrm{i}k_0\vec{r}\cdot\hat{d}}$. Accordingly, the polarization unit vector will be denoted as $\hat{p} = \vec{p}/\,|\vec{p}|$.

For the future developments, it is useful to make explicit the dependence of the far-field pattern on the observation direction $\hat{r}$, the incidence direction $\hat{d}$, the polarization vector of the incident plane wave $\vec{p}$, the supports of the scatterers $\mathbf{D}$ and their relative permittivities $\boldsymbol{\varepsilon}_r$ and electric conductivities $\boldsymbol{\sigma}$. For this reason, the far-field pattern will be denoted as $\vec{E}_\infty(\hat{r}, \hat{d}; \vec{p}; \mathbf{D}; \boldsymbol{\varepsilon}_r, \boldsymbol{\sigma})$. Moreover, in the following, it will be helpful to write the observation direction as

$$\hat{r} = \sin\theta_r \cos\phi_r \hat{x} + \sin\theta_r \sin\phi_r \hat{y} + \cos\theta_r \hat{z}, \tag{5}$$

with $\theta_r \in [0, \pi]$, $\phi_r \in [0, 2\pi)$.

It is worth remarking that, thanks to linearity, $\vec{E}_\infty(\hat{r}, \hat{d}; \vec{p}; \mathbf{D}; \boldsymbol{\varepsilon}_r, \boldsymbol{\sigma}) = |\vec{p}|\, \vec{E}_\infty(\hat{r}, \hat{d}; \hat{p}; \mathbf{D}; \boldsymbol{\varepsilon}_r, \boldsymbol{\sigma})$. Hence, it makes sense to introduce a normalized far-field pattern $\tilde{\vec{E}}_\infty$ such that $\vec{E}_\infty(\hat{r}, \hat{d}; \vec{p}; \mathbf{D}; \boldsymbol{\varepsilon}_r, \boldsymbol{\sigma}) = |\vec{p}|\, \tilde{\vec{E}}_\infty(\hat{r}, \hat{d}; \hat{p}; \mathbf{D}; \boldsymbol{\varepsilon}_r, \boldsymbol{\sigma})$.

As a consequence, by defining $\mathcal{H} = \{(\hat{r}, \hat{d}, \hat{p}) \in \Omega^3 : \hat{p} \cdot \hat{d} = 0\}$, the normalized far–field pattern $\tilde{\vec{E}}_\infty(\ \cdot\ ,\ \cdot\ ;\ \cdot\ ; \mathbf{D}; \boldsymbol{\varepsilon}_r, \boldsymbol{\sigma})$ belongs to the Hilbert space $L_t^2(\mathcal{H}) = \{\vec{f} \in (L^2(\mathcal{H}))^3 : \vec{f} \cdot \vec{n} = 0\}$, where $\vec{n}$ is the normal unit vector to the unit sphere Ω, endowed with the scalar product defined for every $\vec{f}_1, \vec{f}_2 \in L_t^2(\mathcal{H})$ by

$$\begin{aligned}&\left(\vec{f}_1(\cdot)\,,\, \vec{f}_2(\cdot)\right)_{L_t^2(\mathcal{H})} = \\ &\qquad \int_{\mathcal{H}} \vec{f}_1(\hat{r}, \hat{d}; \hat{p}) \cdot \vec{f}_2(\hat{r}, \hat{d}; \hat{p})\, ds(\hat{r}) ds(\hat{d}) ds(\hat{p}).\end{aligned} \tag{6}$$

The aim of this work is to inspect dielectric scatterers starting from the knowledge of the measured far-field pattern $\vec{E}_\infty(\ \cdot\ ,\ \cdot\ ;\ \cdot\ ; \mathbf{D}; \boldsymbol{\varepsilon}_r, \boldsymbol{\sigma})$, by using a two-step hybrid approach which combines the Linear Sampling Method and an Ant Colony Optimization algorithm.

More precisely, in the first stage of the method, the LSM is applied to find an approximation $\mathbf{D}^{retr}$ of the actual supports $\mathbf{D}$ of the scatterers, as detailed in the Section II-A. Subsequently, the Ant Colony Optimization algorithm is used to determine an estimate $\boldsymbol{\varepsilon}_r^{retr}$ and $\boldsymbol{\sigma}^{retr}$ of the relative permittivies $\boldsymbol{\varepsilon}_r$ and the electric conductivities $\boldsymbol{\sigma}$, obtained as

$$(\boldsymbol{\varepsilon}_r^{retr}, \boldsymbol{\sigma}^{retr}) = \underset{(\tilde{\boldsymbol{\varepsilon}}_r, \tilde{\boldsymbol{\sigma}}) \in S}{\operatorname{argmin}}\, \psi(\tilde{\boldsymbol{\varepsilon}}_r, \tilde{\boldsymbol{\sigma}}), \tag{7}$$

where $S \subseteq \mathbb{R}^{2N_{scatt}}$ is the set of the admissible solutions and $\psi : \mathbb{R}^{2N_{scatt}} \to [0, +\infty)$ is the nonlinear cost function defined by

$$\begin{aligned}\psi(\tilde{\boldsymbol{\varepsilon}}_r, \tilde{\boldsymbol{\sigma}}) = \|&\tilde{\vec{E}}_\infty(\ \cdot\ ,\cdot\ ;\ \cdot\ , \mathbf{D}^{retr}, \tilde{\boldsymbol{\varepsilon}}_r, \tilde{\boldsymbol{\sigma}}) \\ &- \tilde{\vec{E}}_\infty(\ \cdot\ ,\cdot\ ;\ \cdot\ , \mathbf{D}, \boldsymbol{\varepsilon}_r, \boldsymbol{\sigma})\|^2_{L_t^2(\mathcal{H})},\end{aligned} \tag{8}$$

where $\|\cdot\|_{L_t^2(\mathcal{H})}$ is the norm induced by the inner product (6).

The implentation of the optimization procedure is explained in Section II-B.

It is worth remarking that this hybrid procedure can be applied to multiple scatterers only if each of them is homogeneous. Furthermore the effectiveness of the method depends on the accuracy with which the LSM provides a visualization of the shape of the scatterer. For example, as it has been shown for the two-dimensional case in [28], the LSM may fail in reconstructing some scatterers whose support is not convex. Moreover, some numerical experiments [29] have shown that the LSM can produce some artifacts when the scatterers are large with respect to the wavelength. Obviously, in such hypotheses the reconstruction of the dielectric permittivity can significantly get worse and the proposed approach can provide unsatisfactory results.

A. The Linear Sampling Method

The starting relation for the description of the LSM is the so called *far-field equation*, which for the three-dimensional vector case reads [9]

$$\int_\Omega \vec{E}_\infty(\hat{r}, \hat{d}; \vec{g}_{\vec{z};\vec{q}}(\hat{d}); \mathbf{D}; \boldsymbol{\varepsilon}_r; \boldsymbol{\sigma}) ds(\hat{d}) = \vec{E}_{e,\infty}(\hat{r}, \vec{z}; \vec{q}), \tag{9}$$

being $\vec{z}$ is a generic point in $\mathbb{R}^3$; $\vec{g}_{\vec{z};\vec{q}}$ is a function in $L_t^2(\Omega)$ for each $\vec{z} \in \mathbb{R}^3$ and $\vec{E}_{e,\infty}(\hat{r},\vec{z};\vec{q})$ is given by [9]

$$\vec{E}_{e,\infty}(\hat{r},\vec{z};\vec{q}) = \frac{\mathrm{i}k}{4\pi}(\hat{r}\times\vec{q})\times\hat{r}e^{-\mathrm{i}k\hat{r}\cdot\vec{z}}. \tag{10}$$

It is worth noting that, thanks to the linearity of (9), we don't loose in generality by setting $|\vec{q}| = 1$; hence in the following it will be assumed $\vec{q} = \hat{q} \in \Omega$.

If we introduce the far-field operator $F : L_t^2(\Omega) \to L_t^2(\Omega)$ defined by

$$\left(F\vec{g}(\cdot)\right)(\hat{r}) = \int_\Omega \vec{E}_\infty(\hat{r},\hat{d},\vec{g}(\hat{d});\mathbf{D};\boldsymbol{\varepsilon}_r;\boldsymbol{\sigma})ds(\hat{d}), \tag{11}$$

the far-field equation (9) can be written as

$$\left(F\vec{g}_{\vec{z};\hat{q}}(\cdot)\right)(\hat{r}) = \vec{E}_{e,\infty}(\hat{r},\vec{z};\hat{q}). \tag{12}$$

At the basis of the linear sampling method there is the following theorem, which holds true for almost all frequency as detailed in [9].

Theorem. *Let F be the far-field operator* (11)*, then:*
1) *if $\vec{z} \in D$, then for every $\epsilon > 0$ there exists a solution $\vec{g}_{\vec{z};\hat{q}}(\cdot) \in L_t^2(\Omega)$ satisfying the inequality*

$$\|(F\vec{g}_{\vec{z};\hat{q}}(\cdot))(\cdot) - \vec{E}_{e,\infty}(\cdot,\vec{z},\hat{q})\|_{L_t^2(\Omega)} < \epsilon, \tag{13}$$

such that

$$\lim_{\vec{z}\to\partial D} \|\vec{g}_{\vec{z};\hat{q}}(\cdot)\|_{L_t^2(\Omega)} = \infty; \tag{14}$$

and

$$\lim_{\vec{z}\to\partial D} \|\vec{v}_{\vec{g}_{\vec{z}}}(\cdot)\|_{L^2(D)} = \infty; \tag{15}$$

2) *if $\vec{z} \notin D$, then for every $\epsilon > 0$ every solution $\vec{g}_{\vec{z};\hat{q}}(\cdot) \in L_t^2(\Omega)$ of the inequality*

$$\|(F\vec{g}_{\vec{z};\hat{q}}(\cdot))(\cdot) - \vec{E}_{e,\infty}(\cdot,\vec{z},\hat{q})\|_{L_t^2(\Omega)} < \epsilon, \tag{16}$$

is such that

$$\lim_{\delta\to 0} \|\vec{g}_{\vec{z};\hat{q}}(\cdot)\|_{L_t^2(\Omega)} = \infty. \tag{17}$$

and

$$\lim_{\delta\to 0} \|\vec{v}_{\vec{g}_{\vec{z}}}(\cdot)\|_{L^2(D)} = \infty; \tag{18}$$

Here

$$\vec{v}_{\vec{g}_{\vec{z}}}(\vec{r}) = \int_\Omega e^{ik\vec{r}\cdot\vec{d}}\vec{g}_{\vec{z}}(\vec{d})ds(\vec{d}) \tag{19}$$

is the Herglotz wave function with kernel $\vec{g}_{\vec{z}}$.

It is worth remarking that analogous theorems hold for scattering problems formulated as exterior problems [9], [22], as when, for example, the scatterer is made up of a perfectly electric conductor or an impedance condition can be written on the boundary of the scatterer itself.

As a consequence of this theorem, there exists an approximate solution of the far-field equation which blows up near the boundary of the scatterers and remains arbitrarly large outside of them: these properties can then be used to visualize the support of the scatterers.

In real experiments, the far-field pattern is measured for M observation directions and N incidence directions, hence a discretized version of the far-field equation (12) is required:

$$\mathbf{F}\mathbf{g}_{\vec{z};\hat{q}} = \mathbf{E}_{e,\infty}(\vec{z};\hat{q}). \tag{20}$$

Here the matrix $\mathbf{F}$ and the two column vectors $\mathbf{g}_{\vec{z};\hat{q}}$ and $\mathbf{E}_{e,\infty}(\vec{z};\hat{q})$ are the discrete counterparts of the far-field operator, the solution and the known term (10), respectively.

In practical applications the far-field pattern is affected by the measurement noise, and therefore only a noisy version $\mathbf{F}^h$ of the far-field pattern is at disposal, such that

$$\mathbf{F}^h = \mathbf{F} + \mathbf{H}, \tag{21}$$

where $\mathbf{H}$ is the noise matrix and $h = \|\mathbf{F}^h - \mathbf{F}\|$. As usual, $\|\cdot\|$ denotes the operator norm of a linear continuous operator.

The linear system (20) is ill-conditioned and the numerical instabilities due to the presence of noise in the measured far-field data can be reduced by applying Tikhonov regularization method, i.e. by determining

$$\mathbf{g}_{\vec{z};\hat{q},\,\alpha} = \underset{\mathbf{g}_{\vec{z};\hat{q}}\in\mathbb{C}^N}{\operatorname{argmin}} \left\{ \left\| \mathbf{F}^h\mathbf{g}_{\vec{z};\hat{q}} - \mathbf{E}_{e,\infty}(\vec{z};\hat{q}) \right\|_M^2 + \alpha \left\| \mathbf{g}_{\vec{z};\hat{q}} \right\|_N^2 \right\}, \tag{22}$$

where we have denoted with $\|\cdot\|_M$ and $\|\cdot\|_N$ the discrete counterpart of the norm induced by the canonical scalar product (3) of $L_t^2(\Omega)$. Proving that (22) has in fact the properties of the approximate solution of the far-field equation described by the previous general theorem is still an open issue. Some hints toward its solution are in [24].

The optimal regularized solution corresponds to the value $\alpha^*_{\vec{z};\hat{q}}$ of the regularization parameter α fixed by means of the generalized discrepancy principle [30], i.e. by finding the zero of the generalized discrepancy function $\rho : (0,+\infty) \to \mathbb{R}$ such that

$$\rho(\alpha) = \left\| \mathbf{F}^h\mathbf{g}_{\vec{z};\hat{q},\,\alpha} - \mathbf{E}_{e,\infty}(\vec{z};\hat{q}) \right\|_M^2 - h^2\|\mathbf{g}_{\vec{z};\hat{q},\,\alpha}\|_N^2. \tag{23}$$

An explicit form for the regularized solution can be determined by using the Singular Value Decomposition (SVD) $\{\sigma_p^h, \mathbf{u}_p^h, \mathbf{v}_p^h\}_{p=1}^{r^h}$ of the far-field matrix $\mathbf{F}^h$. Here r^h is the rank of $\mathbf{F}^h$. In fact, the optimal Tikhonov regularized solution is given by

$$\mathbf{g}_{\vec{z};\hat{q},\,\alpha^*_{\vec{z};\hat{q}}} = \sum_{p=1}^{r^h} \frac{\sigma_p^h}{(\sigma_p^h)^2 + \alpha^*_{\vec{z};\hat{q}}} \left(\mathbf{E}_{e,\infty}(\vec{z};\hat{q}), \mathbf{v}_p^h\right)_M \mathbf{u}_p^h. \tag{24}$$

Here, following the previous notation, $(\cdot,\cdot)_M$ denotes the discrete counterpart of the (3).

According to the previously stated theorem, LSM allows one to visualize the scatterer profile peforming the following steps:

- take a grid $\mathcal{Z} \subset T$, which contains the scatterers;
- for each grid point $\vec{z} \in \mathcal{Z}$, determine the optimal Tikhonov regularized solution (24);
- for each grid point $\vec{z} \in \mathcal{Z}$, consider the quantity $\|\mathbf{g}_{\vec{z};\hat{q},\,\alpha^*_{\vec{z};\hat{q}}}\|_N$

It is worth noting that the norm of $\mathbf{g}_{\vec{z};\hat{q},\,\alpha^*}$ can be analytically expressed in terms of the SVD of the far-field matrix, by exploiting the relation

$$\|\mathbf{g}_{\vec{z};\hat{q},\,\alpha^*_{\vec{z};\hat{q}}}\|_N^2 = \sum_{p=1}^{r^h} \frac{(\sigma_p^h)^2}{\left((\sigma_p^h)^2 + \alpha^*_{\vec{z};\hat{q}}\right)^2} \left| \left(\mathbf{E}_{e,\infty}(\vec{z};\hat{q}), \mathbf{v}_p^h\right)_M \right|^2.$$

The reconstruction is sensitive to the choice of the polarization $\hat{q}$, and numerical experiments have shown that better reconstrucitons are obtained by combining the value of the optimal Tikhonov reglarized solution for three linearly independent versors $\hat{q}$ (see [9], [31]). A correct visualization of the scatterer shape could be obtained by plotting a suitable level surface of the indicator function $\sum_{i=1}^{3} \|\mathbf{g}_{\vec{z};\hat{e}_i,\alpha^*_{\vec{z};\hat{e}_i}}\|_N^{-1}$, where $\hat{e}_i$ represent the i–th element of the canonical basis of $\mathbb{R}^3$.

The output of the LSM is a binary map $\mathcal{B}^{retr}(\vec{z})$ which is equal to 1 if $\vec{z} \in \mathcal{Z}$ belongs to the scatterer, and equal to 0 otherwise. Such a map is obtained by comparing the indicator function with a treshold. In order to quantify the support reconstruction error, it is useful to introduce the error parameter

$$\gamma = \frac{\sum_{\vec{z}\in\mathcal{Z}} |\mathcal{B}^{retr}(\vec{z}) - \mathcal{B}(\vec{z})|}{|\mathcal{Z}|} \tag{25}$$

where $\mathcal{B}(\vec{z})$ is the actual binary map describing the scatterers and $|\mathcal{Z}|$ denotes the cardinality of the set $\mathcal{Z}$.

B. Ant Colony Optimization

The Ant Colony Optimization (ACO) method is a newly introduced stochastic optimization algorithm, which has been inspired by the way ants find the optimal path from their nest to the food [32]. By exploiting these ideas, the ACO method has been initially developed to face hard combinatorial problem, such as the Traveling Salesman Problem and recently it has also been extended to continuous domains [33].

In this section the adopted ACO algorithm is described, which is intended to find the global minimum of the cost function (8) $\psi : \mathbb{R}^{2N_{scatt}} \rightarrow [0, +\infty)$, subjected to the constraint the solution belongs to a set $S \subset \mathbb{R}^{2N_{scatt}}$. For the sake of simplicity, the $U = 2N_{scatt}$ unknowns will be referred to as $\mathbf{x} = [\boldsymbol{\varepsilon}_r \ \boldsymbol{\sigma}]$.

The ACO algorithm faces the constrained global minimization problem by iteratively modifying a population B_l of P trial solutions $\{\mathbf{x}_i^{(l)}\}_{i=1,\ldots,P}$, where the index l denotes the iteration number. The population is stored in an ordered archive, i.e., $\psi(\mathbf{x}_1^{(l)}) \leq \psi(\mathbf{x}_2^{(l)}) \leq \ldots \leq \psi(\mathbf{x}_P^{(l)})$. At each iteration, a set of Q new trial solutions is created. In particular, the U components of a new solution are obtained by sampling a set of U Gaussian kernel Probability Density Functions (PDF), defined as

$$G_j^{(l)}(x) = \sum_{i=1}^{P} w_i \frac{1}{s_{j,i}^{(l)}\sqrt{2\pi}} \exp\left(-\frac{(x - m_{j,i}^{(l)})^2}{2(s_{j,i}^{(l)})^2}\right) \tag{26}$$

where $m_{j,i}^{(l)}$, $s_{j,i}^{(l)}$ and w_i, $i = 1, \ldots, P$, $j = 1, \ldots, U$, are parameters of the PDFs. More specifically, the ACO algorithm is schematized as follows.

- Initialization
- While (termination condition not met) do
  - Ant-based Solution Construction
  - Pheromone Update
- end

The three algorithmic blocks work as follows.

- Initialization: An initial set of P randomly chosen trial solutions $\mathbf{x}_i^{(0)}$, $i = 1, \ldots, P$, is constructed. In particular, the components of $\mathbf{x}_i^{(0)}$ are obtained by sampling a uniform PDF. Furthermore, the Gaussian weights are initialized as

$$w_i = \frac{1}{qP\sqrt{2\pi}} \exp\left(-\frac{(i-1)^2}{2q^2P^2}\right), \quad i = 1, \ldots, P \tag{27}$$

  where q is a parameter of the ACO algorithm.
- Ant-based Solution Construction: First, the parameters of the Gaussian kernel PDFs , $j = 1, \ldots, N$, are updated by using the following relationships

$$m_{j,i}^{(l)} = x_{i,j}^{(l)} \quad i = 1, \ldots, P \quad j = 1, \ldots, U \tag{28}$$

$$s_{j,i}^{(k)} = \xi \sum_{e=1}^{P} \frac{\left|x_{e,j}^{(l)} - x_{j,i}^{(l)}\right|}{l-1} \tag{29}$$

  for $i = 1, \ldots, P$, $j = 1, \ldots, U$, where ξ is the pheromone evaporation rate. Then, Q new trial solution are constructed by sampling the obtained Gaussian kernel PDFs. More precisely, the j-th component of each new trial solution is obtained by sampling the corresponding PDF $G_j^{(l)}$.
- Pheromone Update: The new population B_{l+1} is obtained by adding the newly created trial solutions to the ones contained in the current population B_l and by discarding the worst Q elements.

The algorithm stop when a maximum number of iterations, l_{max}, is reached, or when the cost function value of the best individual is below a fixed threshold, ψ_{th}.

Moreover, in this contribution a modified version of the ACO algorithm has been developed. The devised algorithm, namely Solution Cache ACO (SC-ACO), is based upon the use of a cache of solutions for which the cost function has already been calculated. The modified algorithm works as follows. When a new solution is generated, the cache is searched for a solution $\overline{\mathbf{x}}$ whose all permittivities and conductivities differ from those of the new ones less than d_ε and d_σ, respectively. If sufch a solution is found, then the cost function value is assumed equal to $\psi(\overline{\mathbf{x}})$; otherwise the cost function is actually computed. The SC-ACO algorithm allows a reduction in the number of cost function evaluations, resulting in a speed-up of the imaging method. Clearly, the thresholds d_ε and d_σ may affect the precision with which the optimal solution of the minimization problem can be retrieved.

III. Numerical results

In this section some numerical tests are described in order to validate the proposed approach. In all the considered cases, the far-field pattern is computed by means of the stabilized biconjugate-gradient fast Fourier transform (BCGS-FFT) algorithm [34] and each of the evaluated sample is corrupted by an additivive Gaussian noise of standard deviation equal to the 10% of the actual value. The working frequency is assumed to be equal to 1 GHz.

The far-field pattern has been computed for a uniformly distributed set of incidence and observation directions. More

precisely, it has been evaluated for $\theta_d^n = \frac{\pi}{9}(n+\frac{1}{2})$, $n = 1,\ldots,9$, $\phi_d^m = \frac{\pi}{18}(m+\frac{1}{2})$, $m = 1,\ldots,18$ and $\theta_r^n = \frac{\pi}{9}(n+\frac{1}{2})$, $n = 1,\ldots,9$, $\phi_r^m = \frac{\pi}{18}(m+\frac{1}{2})$, $m = 1,\ldots,18$. Moreover, for every incidence direction two orthogonally polarized waves have been used, namely polarized along $\hat{p}^\theta = \cos\theta_d\cos\phi_d\hat{x} + \cos\theta_d\sin\phi_d\hat{y} - \sin\theta_d\hat{z}$ and $\hat{p}^\phi = -\sin\theta_d\hat{x} + \cos\phi_d\hat{y}$.

In the application of the LSM, all these data have been used, while, in order to make the evaluation of cost function ψ faster, only a subset of them has been employed in the ACO based optimization procedure.

Furthermore, in all the numerical tests presented here, the grid $\mathcal{Z}$ has been obtained by uniformly discretizing the investigation domain T into $31\times31\times31$ points. Such a grid has been used to evaluate the cost function in ACO procedure. The computation time required by LSM to retrieve the shapes of the considered scatterers is about 20 minutes on a PC equipped with a 3 GHz Pentium IV processor and 1 GB of RAM. As concerns the cost function, in the conditions detailed below, it can be evaluated by the same computer by using the BCGS-FFT algorithm in about 35 seconds.

In the first performed tests, a homogeneous dielectric sphere of radius $R_{sp} = 0.075$ m centered at the point of cartesian coordinates $(0, 0.15, 0)$ with reference to different values of the relative dielectric permittivity has been inspected. The considered values of relative dielectric permittivity are: 1.4, 1.7, 2.0, 2.3, 2.6, 2.9 and 3.2. For this case the ACO procedure is responsible for the reconstruction of only one parameter, which is searched in an interval ranging from 1.0 to 7.0. In these numerical tests, we set $T = \{(x,y,z) \in \mathbb{R}^3 : -0.3 \le x \le 0.3, -0.15 \le y \le 0.15, -0.15 \le z \le 0.15\}$ and the ACO algorithm has been applied with a population of $P = 6$ elements, with $Q = 4$, $q = 0.1$ and $\xi = 0.7$, $d_\varepsilon = 0.015$. Moreover, the cost function (8) has been discretized by using waves impinging from directions (θ_d^n, ϕ_d^m), $n = 3,5,7$, $m = 1,10$ and collecting the scattered field along directions (θ_r^n, ϕ_r^m), $n = 3,5,7$, $m = 1,7,13$.

In Table I some data relative to these tests obtained as mean values over 10 runs of the optimization procedure are presented. Namely, the actual relative permittivity ε_r, the support reconstruction error γ (25), the mean reconstructed relative permittivity ε_r^{retr} and the mean number of evaluations of the cost function N_{eval} are reported. Figure 1 shows the shape of the scatterer reconstructed by the LSM for the case $\varepsilon_r = 2$. The reconstructed relative dielectric permittivity and the cost function evaluation number are plotted against the ACO iteration number for a run of the stochastic procedure for the same configuration in Figure 2(a) and 2(b), respectively.

It can be noted that in all the cases the supports and the permittivies are satisfactorily retrieved, although when the permittivity increases the reconstruction becomes slightly worse.

The second considered configuration is composed by a homogeneous parallelepiped which occupies the region $\mathcal{P} = \{(x,y,z) \in \mathbb{R}^3 : -0.1 \le x \le 0.1, -0.05 \le y \le 0.05, -0.075 \le z \le 0.075\}$ and is characterized by a relative dielectric permittivity $\varepsilon_r = 1.6$ and by an electric conductivity $\sigma = 0.1$S/m.

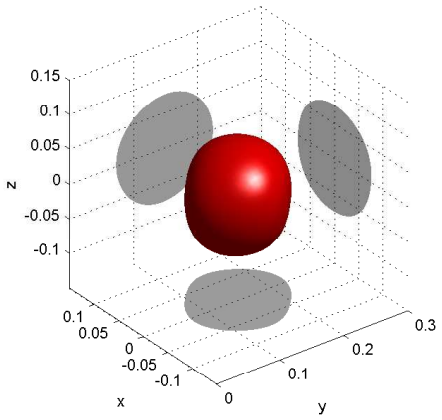

Fig. 1. Reconstructed shape for the case of a homogeneous sphere of relative dielectric permittivity $\varepsilon_r = 2$.

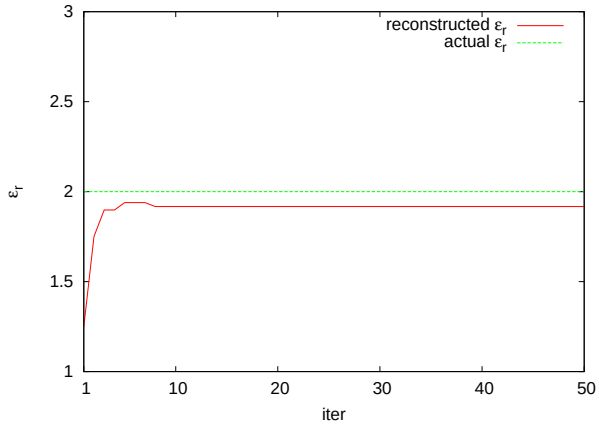

(a) Reconstructed relative dielectric permittivity versus the iteration number.

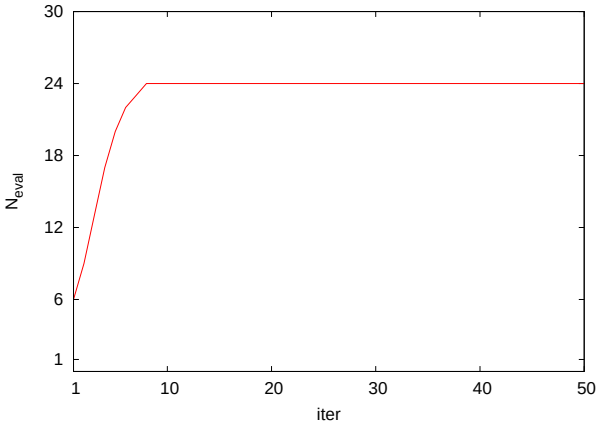

(b) Number of cost function evaluations versus the iteration number.

Fig. 2. Reconstruction of the relative dielectric permittivities of homogeneous dielectric sphere of $\varepsilon_r = 2$ versus the iteration number.

TABLE I
RECONSTRUCTION OF HOMOGENEOUS DIELECTRIC SPHERES

ε_r	γ	ε_r^{retr}	N_{eval}
1.4	0.035	1.38	24.6
1.7	0.031	1.64	21.8
2.0	0.031	1.92	22.3
2.3	0.028	2.15	24.3
2.6	0.026	2.42	21.5
2.9	0.023	2.69	25.3
3.2	0.021	3.13	23.1

TABLE II
RECONSTRUCTION OF A HOMOGENEOUS PARALLELEPIPED

ε_r	σ	γ	ε_r^{retr}	σ^{retr}	N_{eval}
1.6	0.1	0.13	1.56	0.107	45.6

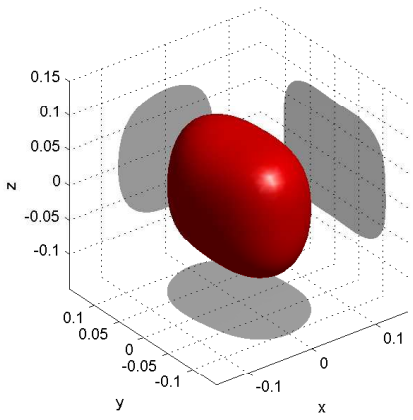

Fig. 3. Reconstructed shape for the case of a homogeneous parallelepiped of relative dielectric permittivity $\varepsilon_r = 2$ and electric conductivity $\sigma = 0.1$S/m.

In this case the relative permittivity is constrained to be in the interval $[1.0, 5.0]$, and the electric conductivity in the interval $[0.0, 0.3]$ S/m. In this case the ACO algorithm has been applied with a population of $P = 12$ elements, with $Q = 8$, $q = 0.1$, $\xi = 0.7$, $d_\varepsilon = 0.05$ and $d_\sigma = 0.005$. Moreover,in application of the LSM, $T = \{(x, y, z) \in \mathbb{R}^3 : -0.15 \leq x \leq 0.15, -0.15 \leq y \leq 0.15, -0.15 \leq z \leq 0.15\}$ has been used. Finally, the same incidence and observation directions have been employed as the previous case for the numerical evaluation of the cost function.

Table II shows the actual relative permittivity ε_r and conductivity σ, the support reconstruction error γ (25), the mean reconstructed relative permittivity ε_r^{retr} and conductivity σ^{retr} and the mean number of evaluations of the cost function N_{eval}. Also in this case, mean values are obtained by averaging the results of 10 runs of the optimization procedure. In Figure 3 the shape of the scatterer retrieved by the LSM is shown.

Figures 4(a) and 4(b) report the reconstructed relative dielectric permittivity and the electric conductivity, respectively, versus the iteration number of the ACO algorithm in a run. Finally, the corresponding cost function evaluation number is shown in Figure 4(c).

In the last test, two cubes, referred to as C_1, C_2, are inspected. The side of both of them measures 0.05 m. The relative permittivity of C_1 is equal to $\varepsilon_{r_1} = 1.8$ and its electric conductivity is $\sigma_1 = 0.15$ S/m. C_2 is instead characterized by $\varepsilon_{r_2} = 2.0$ and $\sigma_2 = 0.1$. C_1 occupies the region $\mathcal{C}_1 = \{(x, y, z) \in \mathbb{R}^3 : -0.175 \leq x \leq -0.125, -0.175 \leq y \leq -0.125, -0.175 \leq z \leq -0.125\}$, whereas the support of C_2 is $\mathcal{C}_2 = \{(x, y, z) \in \mathbb{R}^3 : 0.125 \leq x \leq 0.175, 0.125 \leq y \leq 0.175, 0.125 \leq z \leq 0.175\}$. The LSM has been applied with $T = \{(x, y, z) \in \mathbb{R}^3 : -0.21 \leq x \leq 0.21, -0.21 \leq y \leq 0.21, -0.21 \leq z \leq 0.21\}$ has been used and the ACO algorithm has been used with P = 25, Q = 15, $q = 0.05$, and $\xi = 0.5$. The relative dielectric permittivities are constrined in the range $[1, 3]$, while the electric conductivities in the the interval $[0, 0.3]$ S/m. The cost function (8) has been evaluated by employing incidence directions (θ_d^n, ϕ_d^m), $n = 3, 5, 7$, $m = 1, 7, 13$ and observation directions (θ_r^n, ϕ_r^m), $n = 3, 5, 7$, $m = 1, 4, 7, 10, 13, 16$.

In Figure 5 the supports of the scatterers retrieved by the LSM are shown. The corresponding error parameter (25) is equal to $\gamma = 0.0034$.

Figures 6(a) and 6(b) report the reconstructed relative dielectric permittivities and the electric conductivities, respectively, versus the iteration number of the ACO algorithm in a run. We set $d_\varepsilon = 0.01$ and $d_\varepsilon = 0.001$ for the inspection of this configuration. Finally, the corresponding cost function evaluation number is shown in Figure 6(c). The reconstructed values averaged on 10 runs are the following: $\varepsilon_{r_1}^{retr} = 1.89$, $\sigma_1^{retr} = 0.17$, $\varepsilon_{r_2}^{retr} = 1.80$, $\sigma_2^{retr} = 0.12$. The mean cost function evaluation is equal to $N_{eval} = 53.3$.

IV. CONCLUSION

In this paper a method combining the Linear Sampling Method with Ant Colony Optimization for the inspection of three-dimensional dielectric scatterers has been presented. The proposed approach exploits the strengths of the two methods: the high computational efficiency of the LSM, and the global optimization capabilities of the ACO. Some numerical results validate the described technique.

REFERENCES

[1] D. Colton and P. Monk, "Target identification of coated objects," *IEEE Trans. Antennas Propagat.*, vol. 54, no. 4, pp. 1232–1242, 2006.
[2] L. Xu, E. J. Bond, B. D. V. Veen, and S. C. Hagness, "An overview of ultra wideband microwave imaging via space-time beamforming for early-stage breast-cancer detection," *IEEE Antennas Propagat. Magazine*, vol. 47, no. 1, pp. 19–34, February 2005.
[3] A. Abubakar, P. M. van den Berg, and J. J. Mallorqui, "Imaging of biomedical data using a multiplicative regularized contrast source inversion method," *IEEE Trans. Microwave Theory Tech.*, vol. 50, no. 7, pp. 1761–1771, July 2002.
[4] T. J. Cui, A. A. Aydiner, W. C. Chew, D. L. Wright, and D. V. Smith, "Three-dimensional imaging of buried objects in very lossy earth by inversion of vetem data," *IEEE Trans. Geosci. and Remote Sens.*, vol. 41, no. 10, pp. 2197–2210, October 2003.
[5] R. Zoughi, *Microwave Nondestructive Testing and Evaluation*. The Netherlands: Kluwer Academic Publishers, 2000.

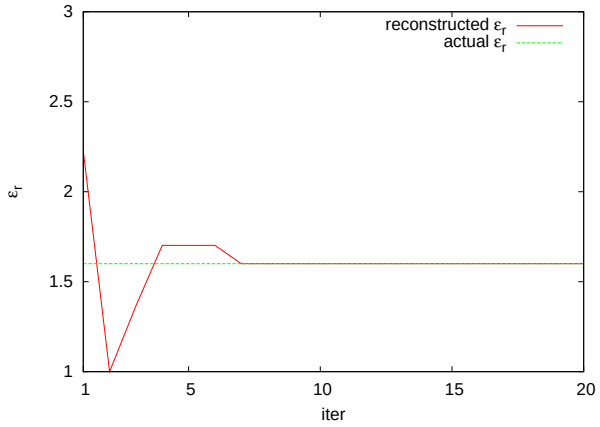

(a) Reconstructed relative dielectric permittivity versus the iteration number.

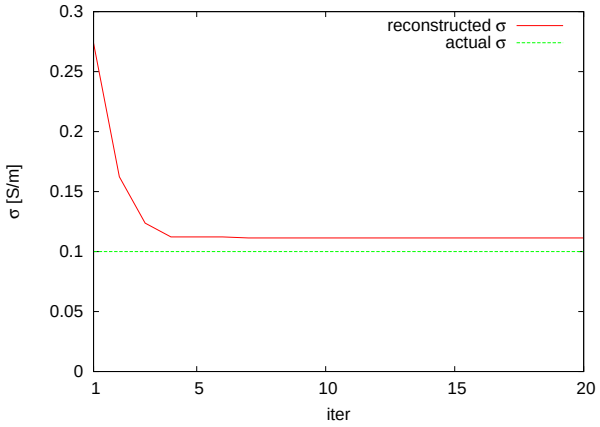

(b) Reconstructed electric conductivity versus the iteration number.

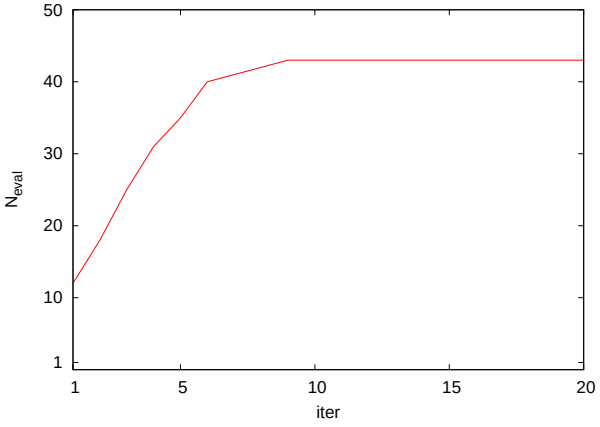

(c) Number of cost function evaluations versus the iteration number.

Fig. 4. Reconstruction of the relative dielectric permittivities and electric conductivity of a homogeneous parallelepiped characterized by $\varepsilon_r = 1.6$ and $\sigma = 0.1$S/m.

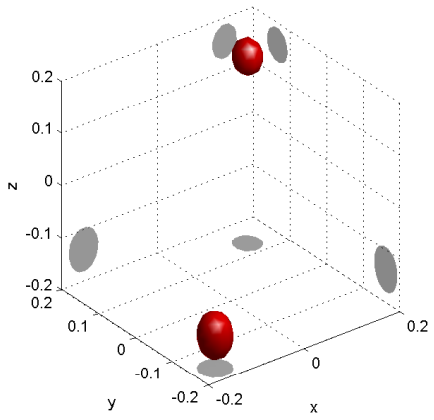

Fig. 5. Supports of two cubes characterized by $\varepsilon_{r_1} = 1.8$ and $\sigma_1 = 0.15$S/m and $\varepsilon_{r_2} = 2$ and $\sigma_2 = 0.1$S/m reconstructed by the LSM.

[6] M. Benedetti, M. Donelli, A. Martini, M. Pastorino, A. Rosani, and A. Massa, "An innovative microwave imaging technique for nondestructive evaluation: Applications to civil structures monitoring and biological bodies inspection," *IEEE Trans. Instrum. Meas.*, vol. 55, no. 6, pp. 1878–1884, December 2006.

[7] D. Colton and A. Kirsch, "A simple method for solving inverse scattering problems in the resonance region," *Inverse Probl.*, vol. 12, pp. 383–393, 1996.

[8] D. Colton, M. Piana, and R. Potthast, "A simple method using morozov's discrepancy principle for solving inverse scattering problems," *Inverse Probl.*, vol. 12, pp. 1477–1493, 1997.

[9] H. Haddar, D. Colton and M. Piana, "The linear sampling method in inverse electromagnetic scattering theory," *Inverse Probl.*, vol. 19, no. 6, pp. S105–S137, 2003.

[10] D. Colton and H. Haddar, "An application of the reciprocity gap functional to inverse scattering theory," *Inverse Probl.*, vol. 21, no. 1, pp. 383–398, 2005.

[11] R. Marklein, K. Mayer, R. Hannemann, T. Krylow, K. Balasubramanian, K. J. Langenberg, and V. Schmitz, "Linear and nonlinear inversion algorithms applied in nondestructive evaluation," *Inverse Probl.*, vol. 18, no. 6, pp. 1733–1759, 2002.

[12] Y. Zhong and X. Chen, "Music imaging and electromagnetic inverse scattering of multiple-scattering small anisotropic spheres," *IEEE Trans. Antennas Propagat.*, vol. 55, no. 12, pp. 3542 – 3549, December 2007.

[13] N. Joachimowicz, C. Pichot, and J. P. Hugonin, "Inverse scattering: an iterative numerical method for electromagnetic imaging," *IEEE Trans. Antennas Propagat.*, vol. 39, no. 12, pp. 1742 – 1753, December 1991.

[14] A. Roger, "Newton-kantorovitch algorithm applied to an electromagnetic inverse problem," *IEEE Trans. Antennas Propagat.*, vol. 2, no. 8, pp. 232–238, February 1981.

[15] O. Franza, N. Joachimowicz, J. -C. Bolomey, "SICS: a sensor interaction compensation scheme for microwave imaging," *IEEE Trans. Antennas Propagat.*, vol. 50, no. 2, pp. 211–216, February 2002.

[16] J. De Zaeytijd, A. Franchois, C. Eyraud, J.-M. Geffrin, "Full-Wave Three-Dimensional Microwave Imaging With a Regularized GaussNewton Method Theory and Experiment," *IEEE Trans. Antennas Propagat.*, vol. 55, no. 11, pp. 3279 – 3292, November 2007.

[17] M. Brignone, J. Coyle, and M. Piana, "The use of the linear sampling method for obtaining super-resolution effects in Born approximation," *J. Comput. Appl. Math.*, vol. 203, pp. 145-158, 2007.

[18] M. Brignone and M. Piana, "The use of constraints for solving inverse scattering problems: physical optics and the linear sampling method," *Inverse Probl.*, vol. 21, pp. 207-222, 2005.

[19] I. Catapano, L. Crocco, M. D'Urso, and T. Isernia "On the Effect of Support Estimation and of a New Model in 2-D Inverse Scattering Problems," *IEEE Trans. Antennas Propagat.*, vol. 55, no. 6, pp. 1895 - 1899, June 2007.

[20] H. Harada, D. J. N. Wall, T. Takenaka, and M. Tanaka, "Conjugate gradient method applied to inverse scattering problem," *IEEE Trans. Antennas Propagat.*, vol. 43, no. 8, pp. 784–792, August 1995.

[21] M. Pastorino, "Stochastic optimization methods applied to microwave

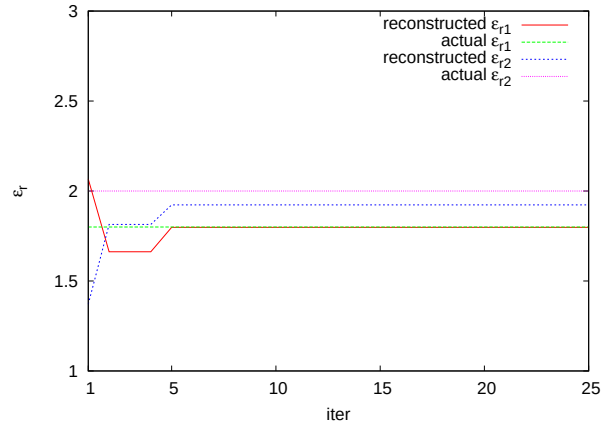

(a) Reconstructed relative dielectric permittivity versus the iteration number.

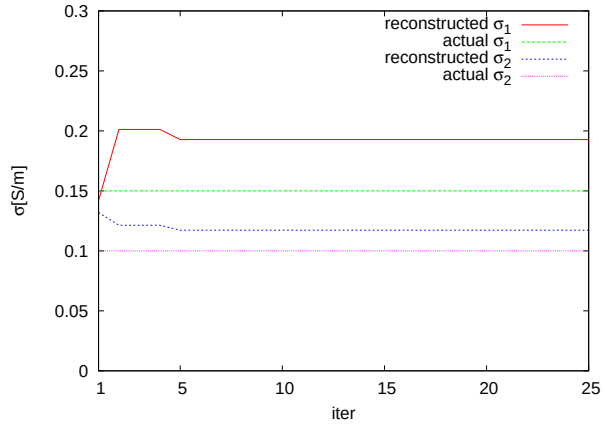

(b) Reconstructed electric conductivity versus the iteration number.

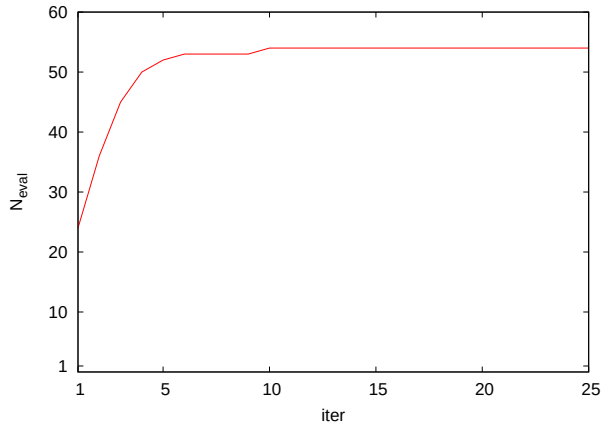

(c) Number of cost function evaluations versus the iteration number.

Fig. 6. Reconstruction of the relative dielectric permittivities and electric conductivity of two cubes characterized by $\varepsilon_{r_1} = 1.8$, $\sigma_1 = 0.15$S/m and $\varepsilon_{r_2} = 2$, $\sigma_2 = 0.1$S/m.

imaging: A review," *IEEE Trans. Antennas Propagat.*, vol. 55, no. 3, Part 1, pp. 538–548, March 2007.

[22] F. Cakoni and D. Colton, *Qualitative methods in inverse scattering theory*. Springer Verlag, 2006.

[23] G. Bozza, M. Pastorino, M. Raffetto, and A. Randazzo, "Synthesis of metamaterial coatings for cylindrical structures by an ant-colony optimization algorithm," in *Proc. 2006 IEEE Int. Workshop on Imagining Systems and Techniques (IEEE IST 2006)*, Minori, Italy, April 29, 2006, pp. 143 – 147.

[24] T. Arens, "Why linear sampling works," *Inverse Probl.*, vol. 20, pp. 163-173, 2004.

[25] R. F. Harrington, *Field Computations by Moment Methods*. New York: MacMillan, 1968.

[26] D. Colton and R. Kress, *Inverse Acoustic and Electromagnetic Scattering Theory*. Berlin: Springer Verlag, 1998.

[27] C. A. Balanis, *Advance Electromagnetic Engineering*. John Wiley & Sons, 1989.

[28] A. Liseno and R. Pierri, "Shape Reconstruction by the Spectral Data of the Far-Field Operator: Analysis and Performances," *IEEE Trans. Antennas Propagat.*, vol. 52, no. 3, pp. 899–903, March 2004.

[29] D. Colton and M. Piana, "The simple method for solving the electromagnetic inverse scattering problem: the case of TE polarized waves", *Inverse Problems* vol. 14, pp. 597-614, 1998.

[30] A. N. Tikhonov, A. V. Goncharsky, V. V. Stepanov, and A. G. Yagola, *Numerical Methods for the Solution of Ill-Posed Problems*. Dordrecht: Kluwer Academic Publishers, 1996.

[31] D. Colton, H. Haddar, and P. Monk, "The linear sampling method for solving the electromagnetic inverse scattering problem," *SIAM J. Sci. Comput.*, vol. 24, pp. 719–731, 2002.

[32] M. Dorigo and L. M. Gambardella, "Ant colony system: A cooperative learning approach to the traveling salesman problem," *IEEE Trans. Evol. Comput.*, vol. 1, no. 1, pp. 53–66, 1997.

[33] K. Socha and M. Dorigo, "Ant colony optimization for continuous domains," *Eur. J. Oper. Res.*, vol. 185, no. 3, pp. 1155–1173, 2008.

[34] Z. Q. Zhang, Q. H. Liu, C. Xiao; E. Ward, G. Ybarra, and W. T. Joines , "Microwave breast imaging: 3-D forward scattering simulation," *IEEE Trans. Biomed. Eng.*, vol. 50, no. 10, pp. 1180 – 1189 , October 2003.